Journal of Materials Chemistry C

PAPER

Cite this: J. Mater. Chem. C, 2019, 7, 5019

A high-performance near-infrared light photovoltaic detector based on a multilayered $PtSe_2$/Ge heterojunction†

Li Wang, Jing-Jing Li, Qi Fan, Zheng-Feng Huang, Ying-Chun Lu, Chao Xie,* Chun-Yan Wu and Lin-Bao Luo *

Received 12th February 2019, Accepted 24th March 2019

DOI: 10.1039/c9tc00797k

rsc.li/materials-c

Light detection in the near-infrared (NIR) region is of particular importance due to its wide application for both military and civil purposes. In this study, we fabricated high-performance NIR photodetectors by simply transferring a multilayered $PtSe_2$ film onto a Ge wafer to form vertical hybrid heterojunctions. These heterojunctions exhibit an apparent photovoltaic effect under NIR illumination, offering our devices the opportunity to operate without an external power supply. Based on further optoelectronic analysis, it was found that the devices were highly sensitive to the 1300, 1550, 1650 and even 2200 nm NIR illumination with good reproducibility and long-term air stability. Under the 1550 nm irradiation, the NIR photodetectors attained the high responsivity and specific detectivity of 602 mA W^{-1} and 6.3 × 10^{11} Jones, respectively, along with fast response speed of 7.4/16.7 μs at zero bias. Due to the excellent photoresponse performance and the simple device geometry, the present self-driven NIR photodetectors are very promising for application in future optoelectronic devices and systems.

Introduction

High-performance cost-effective photodetection has wide potential for applications in both the scientific and industrial fields;[1] to date, researchers have made extensive efforts to develop low-cost and efficient photodetectors based on a number of novel functional materials.[2–4] In particular, in the past few decades, light detection in the near-infrared (NIR, refers to the electromagnetic radiation with the wavelength range from 0.78 to 3.0 μm)[5] region has attracted significant research interest worldwide due to its numerous applications (*e.g.*, in target detection, night vision, surveillance, optical communication, environmental monitoring, remote sensing imaging, and thermal efficiency analysis) in both military and civil areas.[6–9] Currently, the commercially available NIR photodetectors are typically made up of bulk crystalline-Si, which can only respond to the NIR illumination with wavelength shorter than ~1100 nm, as well as Si/Ge heterojunctions or III–V semiconductor alloys (mainly InGaAs and related heterostructures), which operate in the wavelength region beyond the absorption range of crystalline-Si;[10,11] although detectors based on the Si/Ge heterojunctions or III–V semiconductor alloys have already attained excellent NIR photoresponse performance, some inherent problems inevitably hinder the wide applications and future development of these NIR photodetectors.[12–16] For example, high-quality NIR photoactive materials are essentially required for achieving a good photoresponse, which strongly need to be epitaxially grown on some special substrates. In addition, these detectors typically have very complex device architectures and require complicated multistep procedures for construction. Moreover, the use of expensive apparatus for material growth and device fabrication renders these NIR photodetectors uneconomical.

To address the abovementioned difficulties, a promising solution is the development of NIR photodetectors based on other narrow bandgap semiconductors (*e.g.*, HgCdTe, CdSeTe and InSb)[17–19] or topological insulators.[20–22] To date, numerous NIR photodetectors (*e.g.*, Schottky-type photoemissive detectors, quantum dot detectors, and quantum well detectors) with varied device configurations and relatively good device performances have been realized using the abovementioned semiconductors. Another effective avenue involves the integration of traditional narrow bandgap semiconductors, for example, Ge and GaAs, with the emerging two-dimensional (2D) layered materials to assemble hybrid heterojunctions.[23–26] In these heterojunctions, optical absorption occurs primarily in the narrow bandgap semiconductor, and the 2D material usually serves as an active layer for the separation and transport of photocarriers. These hybrid heterostructures are typically characterized by simple device geometries and ease of fabrication, which, therefore,

School of Electronic Science and Applied Physics and Anhui Provincial Key Laboratory of Advanced Materials and Devices, Hefei University of Technology, Hefei, Anhui 230009, China. E-mail: chao.xie@hfut.edu.cn, luolb@hfut.edu.cn

† Electronic supplementary information (ESI) available. See DOI: 10.1039/c9tc00797k

hold great promise for the fabrication of cost-effective NIR photodetectors. For instance, our group has developed NIR photodetectors based on the heterojunctions of chemical vapor deposition (CVD)-grown graphene films and Ge wafers.[27] These devices are highly sensitive to the 1550 nm NIR illumination with the responsivity and specific detectivity reaching 51.8 mA W^{-1} and 1.38 $\times$ 10^{10} Jones, respectively. After this, by taking advantage of the strong light trapping effect of the surface plasmonic nanoparticles and the Ge nanostructure arrays, the responsivity was further increased to as high as 185 mA W^{-1}.[28] Recently, Mahyavanshi *et al.* reported the fabrication of the 2D MoS_2/Ge heterojunction NIR photodetectors, which showed the responsivity of only 16.3 mA W^{-1} upon 1000 nm NIR irradiation.[29] Despite enormous efforts, the performance, especially the responsivity, of these NIR photodetectors is still much lower than that of the commercial Ge NIR photodetectors (typically 850–950 mA W^{-1} at 1550 nm) and, thus, far from satisfactory at the current stage.

In recent years, 2D layered materials, such as graphene and transition metal dichalcogenides (TMDs), have emerged as a class of ideal materials for assembling high-performance photodetectors.[1,11,30,31] Among these materials, group-10 TMDs (*e.g.*, PtS_2, $PtSe_2$, and $PdSe_2$) as a newly discovered 2D material family have attracted extensive attention very recently due to their excellent physical and optoelectronic properties including high carrier mobility, tunable bandgap from 0.25 to 1.6 eV, and superior air stability.[32–37] In particular, the finite bandgap renders the group-10 TMDs extremely attractive for NIR photodetection.[38–43] Herein, we present the development of high-performance NIR photodetectors containing vertical heterojunctions of the multilayered $PtSe_2$/Ge wafer. Owing to the pronounced photovoltaic (PV) effect, the as-prepared heterojunctions can function as self-driven photodetectors operating at zero bias. It was revealed that the heterojunction photodetectors showed high sensitivity to the 1300, 1550, 1650 and even 2200 nm NIR illumination. Specifically, the device exhibited excellent photoresponse properties in terms of the high responsivity of up to 602 mA W^{-1}, the large specific detectivity of 6.3 $\times$ 10^{11} Jones, and the rapid response speed of 7.4/16.7 μs under the 1550 nm irradiation at zero bias. These good performance parameters are close or even comparable to those of the commercial Ge NIR photodetectors. In addition, the devices exhibited respectable reproducibility and long-term air durability. The combination of the abovementioned results together with the simple device architecture renders the present $PtSe_2$/Ge heterojunction photodetectors highly competitive for application in the future efficient and cost-effective NIR photodetection systems.

Results and discussion

Fig. 1(a) and (b) depict the schematic and the optical image of the multilayered $PtSe_2$/Ge heterojunction NIR photodetector, respectively. To facilitate charge carrier collection, a single-layer graphene film was employed as the top electrode. The detailed device fabrication procedure is schematically shown in Fig. S1 (ESI†) and can be found in the Experimental section. In brief, a thin layer of polydimethylsiloxane (PDMS) acting as the insulating

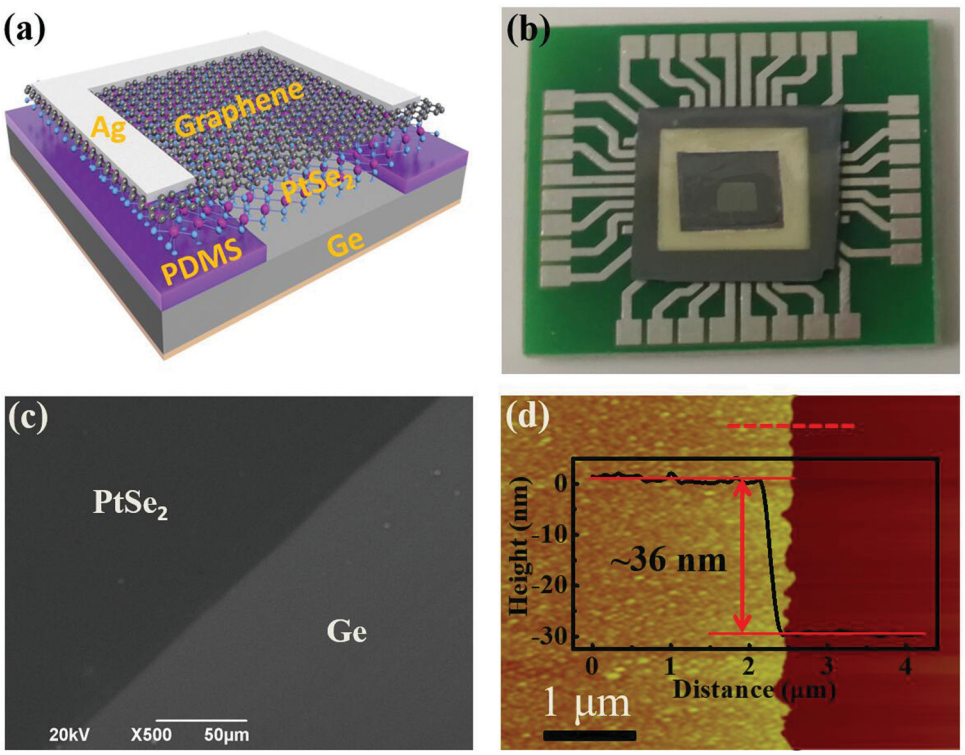

Fig. 1 (a) Schematic of the $PtSe_2$/Ge heterojunction NIR photodetector. (b) An image of the as-prepared photodetector. (c) An SEM image of the multilayered $PtSe_2$ on the Ge substrate. (d) An AFM image of the as-synthesized $PtSe_2$ layer. The inset shows the height profile.

layer was obtained first by spin-coating a PDMS solution onto a pre-cleaned Ge substrate, and a rectangular area of the PDMS was removed to define the effective area of the device. Then, multilayered $PtSe_2$ and the single-layer graphene films were sequentially transferred onto the substrate. Finally, the Ag electrode was deposited *via* electron beam evaporation using a lab-built shadow mask, and the In–Ga alloy was attached to the rear side of the Ge substrate to obtain the top and the bottom electrical contacts. In this study, the multilayered $PtSe_2$ film was synthesized *via* selenization of the pre-deposited Pt thin films according to a previous study.[44] Fig. 1(c) shows a typical field emission scanning electron microscopy (FESEM) image of the $PtSe_2$ layer transferred onto the Ge substrate. Apparently, the large-scale continuous $PtSe_2$ layer with respectable uniformity was clearly observed, and the boundary of the film could also be distinguished due to the difference in contrast. The thickness of the as-prepared $PtSe_2$ layer was about 36 nm, as determined by the atomic force microscopy (AFM) image displayed in Fig. 1(d). As a result, due to its relatively large thickness, the multilayered $PtSe_2$ used in this study can be considered a semimetal.[44] Furthermore, Raman analysis revealed two representative peaks located at 177 and 206 cm^{-1} (Fig. S2a, ESI†), which corresponded to the E_g in-plane vibrational mode of the Se atoms and the A_{1g} out-of-plane vibration mode, respectively.[36] In addition, the X-ray photoemission spectroscopy (XPS) analysis was performed to investigate the components and the binding energy of the as-prepared sample. As plotted in Fig. S2b and c (ESI†), two peaks corresponding to the Pt $4f_{7/2}$ and Pt $4f_{5/2}$ orbitals were observed at 73.34 and 76.67 eV, respectively, whereas the peaks at 54.72 and 55.47 eV corresponded to the Se $3d_{5/2}$ and Se $3d_{3/2}$ orbitals of the divalent selenium ions.[38] The abovementioned results coincide well with those obtained for the $PtSe_2$ multilayers in previous studies;[35,38] this suggests that the large-scale multilayered $PtSe_2$ film with good quality has been successfully synthesized.

The operational mechanism of our $PtSe_2$/Ge heterojunction NIR photodetector can be illustrated *via* analysis of the energy band diagram and carrier transport process of the heterojunction. According to a previous study, the Fermi level (E_F) of multilayered $PtSe_2$ with semimetallic features was calculated to be ~4.84 eV.[44] In addition, the work function of n-Ge with the resistivity of 1–10 Ω cm was roughly deduced to be ~4.37 eV.[45] Therefore, due to the disparity in the work functions, electrons will diffuse from Ge to $PtSe_2$, leaving positively charged empty states within the depletion region in Ge until their Fermi levels align, when the two materials communicate with each other. This charge transfer results in the upward bending of the energy levels near the Ge surface and the emergence of a built-in electric field. Similar to the cases of many graphene/Si heterojunctions,[23] upon illumination with a photon energy exceeding the bandgap of Ge (~0.67 eV), electron–hole pairs are produced within the depletion region in Ge. These carriers, generated in the vicinity of the depletion region, can also diffuse to the depletion region. Subsequently, the electrons and holes are quickly separated by the built-in electric field, and the electrons are collected by the bottom In–Ga electrode, whereas the holes transfer across $PtSe_2$ and the graphene stacked layers and are ultimately collected by the Ag electrode. The abovementioned processes give rise to the generation of photocurrent at zero bias. Note that due to the optical absorption of multilayered $PtSe_2$ in the NIR region, under the incident NIR illumination possessing a photon energy lower than the bandgap of Ge and higher than the heterojunction barrier height ($\Phi_B < h\nu < E_g$), the electrons generated within $PtSe_2$ will have enough energy to surpass the barrier and inject into the conduction band of Ge, which also contribute to the photocurrent.

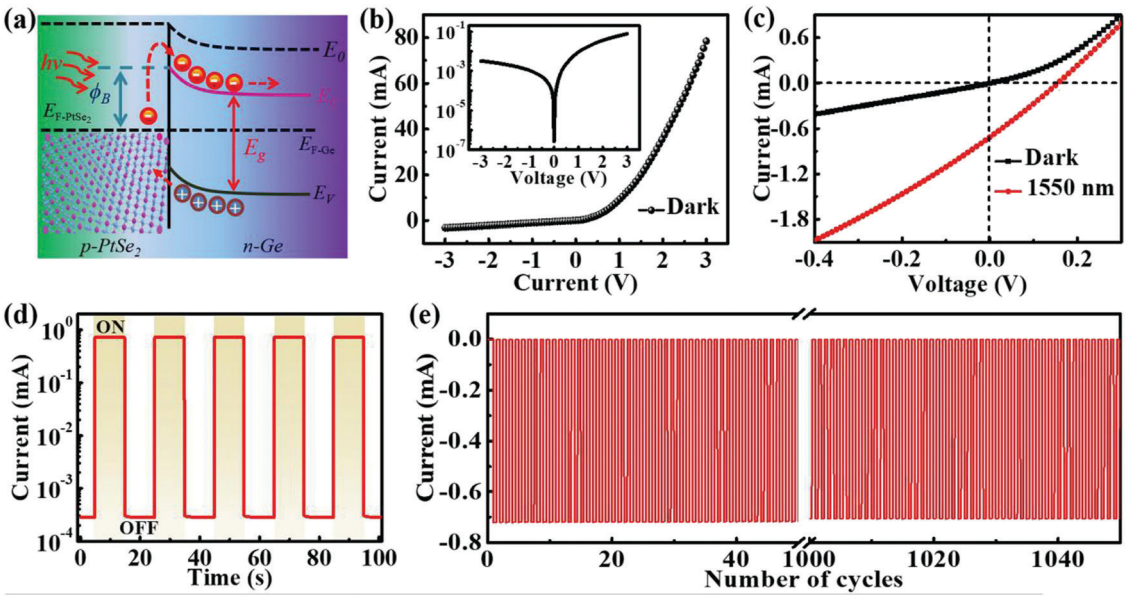

Fig. 2 (a) Energy band diagram of the $PtSe_2$/Ge heterojunction under NIR illumination. (b) *I*–*V* curve of the $PtSe_2$/Ge heterojunction device in the dark. Inset shows the *I*–*V* curve on a semilogarithmic scale. (c) Comparison of the *I*–*V* characteristics of the heterojunction device in the dark and under 1550 nm NIR illumination (4.3 mW). Time-dependent photoresponse of the device (d) under periodically switched 1550 nm illumination and (e) over thousands of cycles of operation.

In other words, the introduction of multilayered $PtSe_2$ is expected to extend the detection limit of the Ge NIR photodetectors towards longer wavelengths.

To verify the abovementioned proposed working mechanism, we characterized the optoelectronic properties of the $PtSe_2$/Ge heterojunctions. The current–voltage (*I–V*) curve of the device was first obtained in the dark, as shown in Fig. 2(b). Clearly, an obvious current rectifying behavior with the rectification ratio of ~25 at ±3 V was observed. Since graphene and the In–Ga alloy can form good Ohmic contacts with the $PtSe_2$ layer and the Ge substrate, respectively (Fig. S3, ESI†), the abovementioned rectifying effect should exclusively originate from the heterojunction between $PtSe_2$ and Ge. Fig. 2(c) shows a comparison of the *I–V* characteristics observed in the dark and under 1550 nm NIR illumination (4.3 mW). It can be easily observed that the heterojunction exhibits a pronounced PV activity with the open-circuit voltage (V_{OC}) of 156.1 mV and the short-circuit current (I_{SC}) of 0.71 mA, leading to the power conversion efficiency (PCE) of ~0.67%. Although the PCE is rather low, this PV effect endows our heterojunction with an opportunity to function as a self-driven photodetector operating at zero bias. Further time-dependent photoresponse revealed that the device presented a repeatable and stable response to periodically switched NIR illumination with well distinguished low- and high-conductance states at zero bias (Fig. 2(d)). The response curve has very steep rise and fall edges, implying that the built-in electric field can rapidly separate the photoexcited electrons and holes. In addition, our detector exhibited excellent reproducibility, as confirmed by the repeatable photoresponse even after thousands of cycles of operation (Fig. 2(e)).

The light power-dependent photoresponse properties of the $PtSe_2$/Ge heterojunction were further studied. Fig. 3(a) and (b) show the *I–V* curves obtained under varied NIR illumination conditions with the power ranging from 5 μW to 3.61 mW. Significantly, both the photovoltage and the photocurrent at zero bias increased monotonously with an increase in the light power due to the increase in the amount of photocarriers under illumination with a higher power. Careful analysis revealed that the photovoltage first increased rapidly from 2.82 to 123.7 mV when the light power was changed from 5 μW to 0.82 mW, whereas a further increase in the light power from 0.82 to 3.61 mW only led to a slow increase in the photovoltage from 123.7 to 156.1 mV, as shown in Fig. 3(c). As supposedly determined by the Fermi level disparity between two materials, the uppermost photovoltage, theoretically attained by the present $PtSe_2$/Ge heterojunction, should be ~470 meV. Therefore, further improvement of the device performance can be accomplished by optimizing the heterojunction interface, electrical contact and so on.[46] In addition, a similar evolution of the light power-dependent photocurrent was observed. To shed light on this dependence, the curve of photocurrent at zero bias *versus* light power was fitted with the general power law: $I_{ph} = AP^{\theta}$, where I_{ph}, A, and P represent photocurrent, a constant related to the light wavelength, and the incident light power, respectively, and the exponent θ is an empirical value reflecting the photocarrier recombination activity.[47] As depicted in the inset of Fig. 3(c), fitting of the curve provided two distinct exponent values: θ = 0.86 for the low power region and θ = 0.54 for the high power region. The abovementioned result manifested that a relatively weaker recombination loss occurred in the low-power region, whereas it became stronger in the high-power region. This phenomenon was attributed to the intensified charge carrier recombination due to higher concentration of the photogenerated

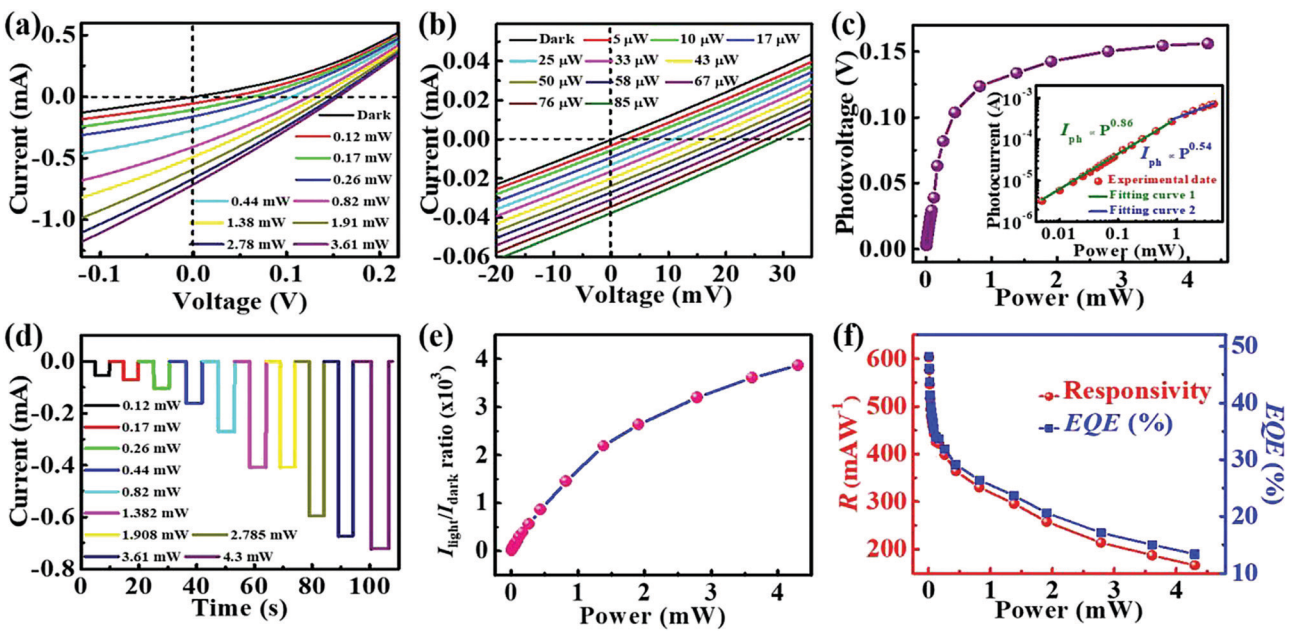

Fig. 3 (a and b) Depict the *I–V* curves of the $PtSe_2$/Ge heterojunction device under the 1550 nm illumination with varied light power. (c) Photovoltage as a function of light power. Inset shows the photocurrent at zero bias as a function of light power. (d) Time-dependent photoresponse of the device under the 1550 nm illumination with varied light power. Dependence of (e) I_{light}/I_{dark} ratio and (f) responsivity and EQE on the incident light power.

carriers at a higher power as well as the presence of some trap states within the Fermi level and the conduction band edge.[46] Time-dependent photoresponse at zero bias was also obtained at different light powers, as shown in Fig. 3(d). Clearly, the detector can be readily switched between the on- and the off-states under all the illuminating conditions; this implies that the present NIR photodetector can operate properly under irradiation in a broad light power region. In addition to photovoltage and photocurrent, the I_{light}/I_{dark} ratio was observed to increase gradually with an increase in light power, and the maximum value reached 3.8×10^3 at the light power of 4.3 mW (Fig. 3e). Note that the maximum I_{light}/I_{dark} ratio was expected to reach as high as $\sim 2.3 \times 10^4$ since the active device area (0.06 cm^{-2}) was much larger than the effective illuminating area (0.01 cm^{-2}); thus, the dark current was overestimated.

The thickness dependence of the $PtSe_2$ layers on the NIR photoresponse properties was studied. Fig. S4a (ESI†) shows the *I–V* curves of the $PtSe_2$/Ge heterojunctions with different $PtSe_2$ thicknesses of ~11, ~18, ~29 and ~36 nm. It was observed that all samples displayed photovoltaic behavior under the 1550 nm NIR illumination irrespective of the $PtSe_2$ thickness. However, with the gradually increasing $PtSe_2$ thickness, the photocurrent was found to significantly increase from 0.087 mA, 0.27 mA, 0.42 mA to 0.71 mA. This evolution of the photocurrent with the $PtSe_2$ thickness would be primarily ascribed to the difference in the charge carrier transport and collection capabilities of $PtSe_2$ and graphene electrode since the sheet resistance of the $PtSe_2$ layers decreases monotonously with an increase in their thickness (Fig. S4b, ESI†). Considering the difficulty of achieving successful selenization upon further increasing the thickness of the precursor Pt film, the $PtSe_2$ thickness was optimally selected to be ~36 nm in our study.

To facilitate the comparison of the photoresponse performance of different NIR photodetectors, some key performance figures-of-merit including responsivity (*R*), external quantum efficiency (EQE) and specific detectivity (*D**) were calculated. The *R* is described as the ratio of the output photocurrent to the incident optical power on the active region of the photodetector, whereas EQE is ratio of the number of photogenerated electron–hole pairs with contribution to photocurrent and the number of incident photons. The two parameters are usually expressed as follows:[30]

$$R = \frac{I_{ph}}{P_\lambda} = \mathrm{EQE}\left(\frac{e\lambda}{hc}\right)G, \quad (1)$$

where I_{ph}, P_λ, e, λ, h, c and G represent the photocurrent ($I_{ph} = I_{light} - I_{dark}$), the incident light power, the elementary charge, the wavelength of light, the Planck's constant, the velocity of light and the photoconductive gain, respectively. The value of G is unity in a PV-type detector in the absence of the internal gain mechanism.[1] Therefore, based on these equations, the *R* and EQE were deduced to be 602 mA W^{-1} and 48.2%, respectively, at a low light power (5 μW) under zero bias. This large *R* value is significantly higher than those of the NIR photodetectors based on graphene/Ge (51.8 mA W^{-1}),[27] plasmon enhanced graphene/Ge nanoneedle array (185 mA W^{-1}),[28] $PtSe_2$/Si (0.57 mA W^{-1}),[48] the $PtSe_2$/CdTe nanowire (~33 mA W^{-1}) at zero bias,[49] and MoS_2/Ge (16.3 mA^{-1}) at the bias of −5 V[49] and is close to that of the commercially available Ge NIR photodetectors (850–950 mA^{-1}) (see Table 1). Moreover, as plotted in Fig. 3(f), both *R* and EQE were found to decline gradually with an increase in light power; this again verified the existence of a nonnegligible recombination loss in the present NIR photodetector at a high light power.

In addition, the value of *D** reflects the ability of a photodetector to measure the minimum optical signal and is usually described by the following equation:

$$D^* = \frac{RA^{1/2}}{(2eI_d)^{1/2}}, \quad (2)$$

where *A* is the effective device area (0.06 cm^{-2}), and I_d denotes the dark current. According to these values, *D** was estimated to be 6.3×10^{11} Jones at zero bias, which was higher than that of the commercial Ge NIR photodetectors (2.5×10^{11} Jones) (see Table 1).

To gain insight into the dependence of the photoresponse on the incident light wavelength, we studied the photoresponse under illumination of varied wavelengths at a constant optical power (4.3 mW), as shown in Fig. 4(a). It was observed that while the dark current remained nearly the same under illumination of different wavelengths (Fig. S5, ESI†), the photoresponse first increased gradually with an increase in the incident light wavelength and then declined significantly upon further increasing the light wavelength. The maximum photoresponse was found at around 1550 nm. Additionally, the present photodetector exhibited a rather weak photoresponse in the visible light region. To deeply understand the wavelength-dependent photoresponse, time-dependent photoresponse at other NIR illumination wavelengths was further investigated. Fig. 4(b) shows the photoresponse of the device upon illumination with the periodically switched 1300 and 1650 nm

Table 1 Comparison of the device performance of the NIR photodetectors used in this study with those reported in the literature along with typical commercial Ge NIR photodetectors

Device structure	*R* (mA W^{-1})	τ_r/τ_f (μs)	I_{light}/I_{dark} ratio	*D** (Jones)	Measurement conditions	Ref.
$PtSe_2$/Ge	602	7.42/16.71	3.8×10^3	6.31×10^{11}	V_{bi} = 0 V, λ = 1550 nm	This study
Graphene/Ge	51.8	23/108	1×10^4	1.38×10^{10}	V_{bi} = 0 V, λ = 1550 nm	27
ITONPs@SLG/GeNNs array	185	0.45/0.46	5×10^4	2.28×10^{13}	V_{bi} = 0 V, λ = 1550 nm	28
MoS_2/Ge	16.3	—	~7	—	V_{bi} = −5 V, λ = 1000 nm	29
$PtSe_2$/CdTe	~33	8.1/43.6	~5	$\sim 2.7 \times 10^{10}$	V_{bi} = 0 V, λ = 1550 nm	49
$PtSe_2$/Si	0.57	55.3/170.5	5×10^2	$\sim 3 \times 10^{10}$	V_{bi} = 0 V, λ = 1550 nm	48
Commercial (Ge-FDG50)	850	0.22/0.22	—	2.5×10^{11}	λ = 1550 nm	
Commercial (Ge-FDG10X10)	950	10/10	—	2.5×10^{11}	λ = 1550 nm	

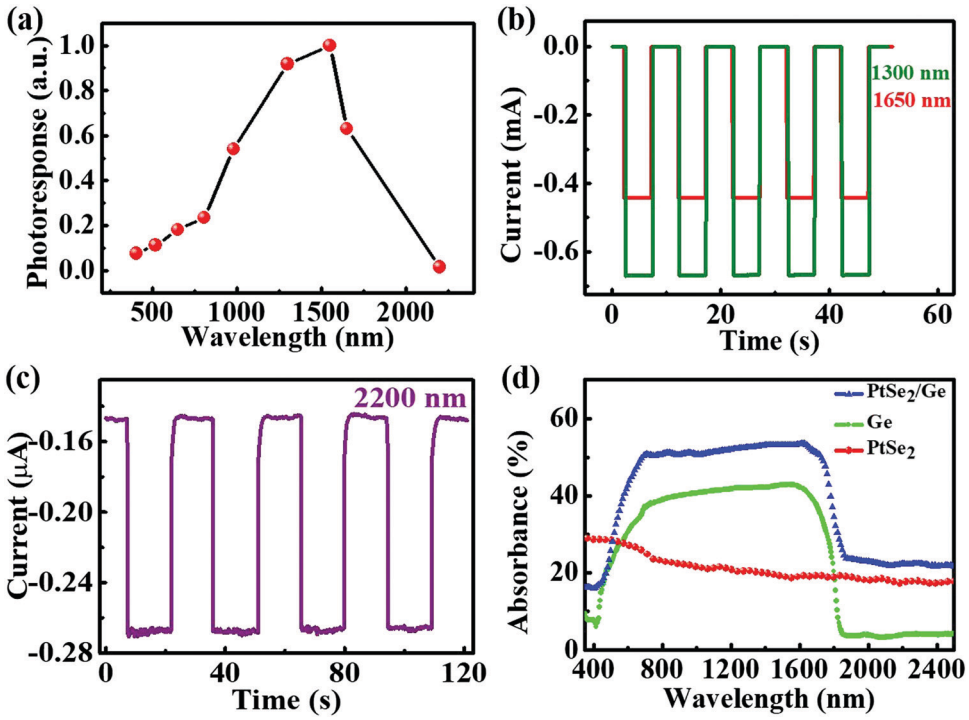

Fig. 4 (a) Wavelength-dependent photoresponse of the $PtSe_2$/Ge heterojunction photodetector. Time-dependent photoresponse of the device under (b) 1300 nm (4.3 mW) and 1650 nm (4.3 mW), and (c) 2200 nm (0.94 mW) NIR illumination at zero bias. (d) Absorption spectra of the $PtSe_2$ film, Ge substrate, and $PtSe_2$/Ge hybrid.

light with a fixed light power (4.3 mW). Clearly, the device can respond stably and repeatedly to these illuminations. Comparatively, the photoresponse at 1550 nm was highest (Fig. 2(d)), which was related to the intrinsic absorption property of Ge (Fig. 4(d)) and also in good accordance with the results shown in Fig. 4(a). The R values were calculated to be $\sim$560 mA W^{-1} and $\sim$381 mA W^{-1} for the 1300 and 1650 nm wavelengths, respectively. Interestingly, we observed that the present photodetector was also sensitive to the NIR illumination beyond the intrinsic absorption limit of Ge ($\sim$1850 nm). For example, as depicted in Fig. 4(c), the detector was capable of showing a repeatable and stable response to the 2200 nm illumination with a relatively weak power (0.94 mW, limited by the light source in our lab). This NIR photoresponse can be directly related to the strong light absorption of multilayered $PtSe_2$ in this wavelength region (Fig. 4(d)) and is expected as discussed in the abovementioned energy band diagram analysis section. It was expected that the NIR photoresponse beyond $\sim$1850 nm could be further improved by optimizing the optical absorption of $PtSe_2$ *via* defect engineering by controlling the material growth conditions and/or plasma treatments[35] and integration with plasmonic nanostructures resonated in the NIR regime.[50]

Furthermore, we have studied the response speed of our NIR photodetector, which is a key parameter reflecting the ability of the device to follow a fast varying optical signal. Fig. 5(a) illustrates the setup of the response speed measurement in our experiment. The detector was exposed to high-frequency pulsed NIR illumination produced by the 1550 nm laser diode powered by a signal generator, and the variation of photoresponse (photovoltage *versus* time) was determined using an oscilloscope. Fig. 5(b)–(d) and Fig. S6 (ESI†) depict the photoresponse of the detector to the pulsed light with varied modulation frequencies of 0.2, 20, 50 and 100 kHz, respectively. Remarkably, at all these frequencies, the NIR photodetector was able to show excellent switching properties with good stability and repeatability. Even at the high frequency of 100 kHz, although the photoresponse degraded somewhat, the device could still exhibit distinct low and high photovoltage states, indicating a fast response speed. The dependence of the relative balance $(V_{max} - V_{min})/V_{max}$ of the photoresponse on the modulation frequency was further summarized and is plotted in Fig. 5(e). It was revealed that the relative balance showed a slow decay with an increase in the switching frequency, and the value declined by $\sim$70% at the very high frequency of 100 kHz. In addition, the 3 dB bandwidth that represents the frequency at which the photoresponse declines to 70.7% of its peak value has been determined to be $\sim$52 kHz. Finally, the response times were calculated using the magnified photoresponse curve obtained at 50 kHz. As depicted in Fig. 5(f), the rise and fall times were deduced to be 7.4 and 16.7 μs, described by the time interval required for the photoresponse to increase/drop from 10%/90% to 90%/10% of its maximum value, respectively.[51] Notably, the response speed was comparable to that of a number of Ge-based NIR photodetectors described in the literature[27,49] and even to that of the commercial Ge NIR photodetectors (see Table 1). This high response speed can be ascribed directly to a special device geometry, which is beneficial for the rapid separation and transport of photogenerated charge carriers. These results suggested that the present photodetector was capable of monitoring high-frequency NIR

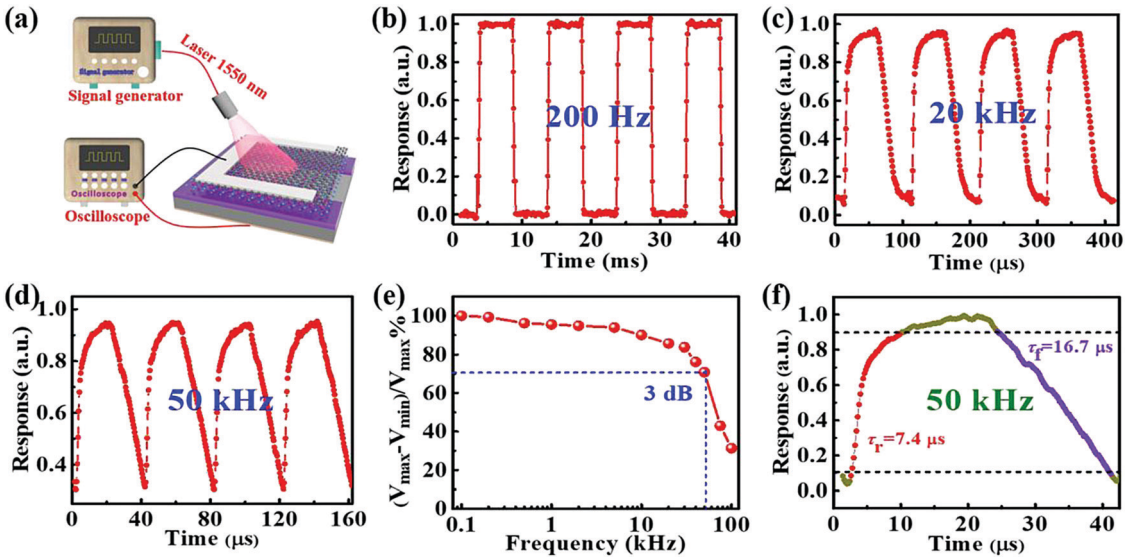

Fig. 5 (a) Schematic of the setup for the response speed measurements. The photoresponse of the heterojunction device under the pulsed 1550 nm illumination at a frequency of (b) 200 Hz, (c) 20 kHz and (d) 50 kHz. (e) Relative balance $(V_{max} - V_{min})/V_{max}$ as a function of the switching frequency of the incident light, showing 3 dB cutoff frequency of ~52 kHz. (f) A single magnified photoresponse curve for deducing the rise and fall times.

optical signals and therefore held great promise for high-speed NIR photodetection.

To explore the possibility of practical application, the air durability of the present NIR photodetector was examined by placing the sample under ambient conditions without any protection for 3 months. As shown in Fig. 6(a) and (b), the device exhibited no obvious degradation in both the rectifying behavior and the photoresponse properties after storage. In addition, according to the photoresponse curve at 50 kHz, the response speed remained nearly unchanged after storage (Fig. 6(c)). The above-mentioned results suggested superior long-term air stability and durability of the NIR photodetector, which was ascribed to the following two phenomena. First, as reported previously,[44] the multilayered $PtSe_2$ film possessed excellent air stability,

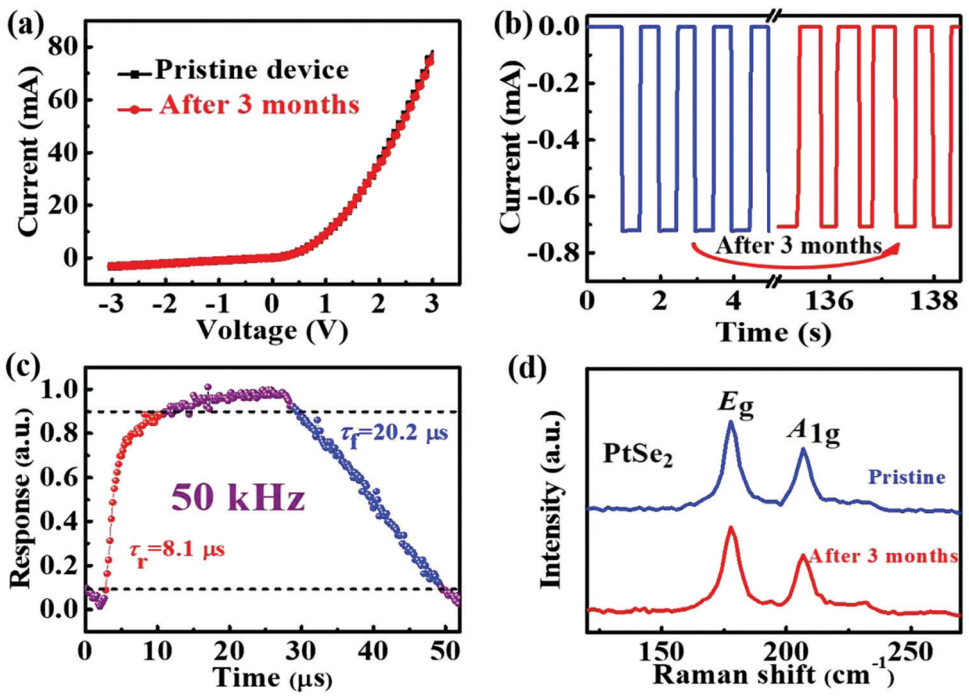

Fig. 6 (a) I–V curves and (b) time-dependent photoresponse of the $PtSe_2$/Ge heterojunction photodetector before and after the storage under ambient conditions for 90 days. (c) A single magnified photoresponse curve for estimating rise and fall times of the device after the storage for 90 days. (d) Raman spectra of the $PtSe_2$ layer before and after the storage for 90 days.

which was further manifested by the almost identical Raman spectra of the sample before and after storage for 3 months (Fig. 6(d)). Second, the relatively thick and compact multilayered film maintained the high quality of the heterojunction interface by preventing oxidation on the Ge surface.

Experimental

Material preparation and characterization

The multilayered $PtSe_2$ used in this study was synthesized *via* a simple selenization method described in a previous study.[38] At first, a ~10 nm Pt precursor film was deposited on the pre-cleaned SiO_2/Si substrate using electron-beam evaporation. Then, the Pt-coated substrate was placed in the central zone of a tube furnace, and selenium powder (99.99% purity) was loaded in the upstream side. The powder was heated to ~220 °C and the evaporated gas was carried by a 50 sccm argon gas flow. The substrate was heated to ~450 °C. After reaction for 1 h, the grey multilayered $PtSe_2$ film was obtained on the substrate.

The morphology and the topography of the as-prepared $PtSe_2$ layer were observed using FESEM (Hitachi, SU8020) and AFM (Benyuan Nanotech Com, CSPM-4000), respectively. The Raman spectra of samples were measured using an HR Evolution (Horiba Jobin Yvon) Raman spectrometer equipped with a 532 nm laser. The XPS measurements were conducted using a monochromatic Al Kα source (1486.6 eV) produced by the XPS system. The absorption spectra of the multilayered $PtSe_2$, the Ge substrate, and the $PtSe_2$/Ge hybrid were recorded using a Shimadzu UV-2550 UV-vis spectrophotometer.

Device fabrication and analysis

To construct the $PtSe_2$/Ge heterojunction photodetector, the n-type Ge substrate (resistivity: 1–10 Ω cm^{-1}) was first ultrasonically cleaned with acetone, ethanol, and deionized (DI) water sequentially. Then, a PDMS solution was spin-coated onto the substrate to obtain a thin layer of PDMS, which serves as the insulating layer. The exposed Ge window area (0.2 × 0.3 cm^2) was obtained by removing the upper layer PDMS with the help of a graver, which defines effective area of the heterojunction device. The $PtSe_2$ layer on the SiO_2/Si substrate was spin-coated with 5 wt% polymethylmethacrylate (PMMA) in chlorobenzene, and then the underlying oxide was removed using an alkali solution. After rising with DI water several times to remove the residual ions, the $PtSe_2$ layer was transferred onto the above substrate. Afterwards, the PMMA on $PtSe_2$ was removed using acetone. Similarly, a chemical vapor deposition grown single-layer graphene film was transferred onto the $PtSe_2$ by using the PMMA-assisted transfer method.[52] Finally, the 50 nm Ag electrode, which serves as the top electrical contact, was deposited on graphene using a lab-built shadow mask *via* electron-beam evaporation. The bottom electrical contact for n-Ge was obtained by attaching the In–Ga alloy to the rear side of the substrate.

The electrical measurements were conducted using a semiconductor characterization system (4200-SCS, Keithley Co. Ltd). To study the photoresponse, NIR laser diodes with different wavelengths (Thorlabs, M1300L3, M1550L3, M1650L3, and MDL-H-2200) were used as the light sources. For the response speed measurements, a signal generator (Tektronix, TDS2022B) was employed to drive the laser diode to produce pulsed NIR irradiation with different frequencies, and an oscilloscope (Tektronix, TDS2012B) was used to record the electrical output. The light power of all the light sources was carefully calibrated using a power meter (Thorlabs GmbH., PM 100D) prior to use. All measurements were conducted under ambient conditions at room temperature.

Conclusions

In summary, we have reported high-performance NIR photodetectors, which are basically composed of multilayered $PtSe_2$/Ge vertical hybrid heterojunctions. The as-prepared heterojunctions exhibited pronounced PV activity under the NIR illumination, which allowed our devices to function as self-driven photodetectors without an external energy supply. The optoelectronic analysis revealed that the devices displayed high sensitivity to the 1550 nm illumination with the high responsivity of up to 602 mA W^{-1}, the large specific detectivity of 6.3×10^{11} Jones, and the fast response speed of 7.4/16.7 μs at zero bias. In addition, the detectors were sensitive to the other NIR illuminations including the 1300 and 1650 nm irradiation, and even to the 2200 nm illumination beyond the absorption cutoff wavelength of Ge due to the strong absorption of multilayered $PtSe_2$. Considering the outstanding photoresponse performance, the simple device geometry and the excellent long-term air durability, it is expected that the present $PtSe_2$/Ge heterojunction NIR photodetectors can find important applications in future air-stable, cost-effective and efficient NIR photodetection.

Conflicts of interest

There are no conflicts to declare.

Acknowledgements

This work was supported by the National Natural Science Foundation of China (NSFC, No. 61575059, 61675062, 21501038) and the Fundamental Research Funds for the Central Universities (No. JZ2018HGPB0275, JZ2018HGTA0220, JZ2018HGXC0001).

References

1 F. H. L. Koppens, T. Mueller, P. Avouris, A. C. Ferrari, M. S. Vitiello and M. Polini, *Nat. Nanotechnol.*, 2014, **9**, 780–793.
2 G. Konstantatos, M. Badioli, L. Gaudreau, J. Osmond, M. Bernechea, F. P. G. de Arquer, F. Gatti and F. H. L. Koppens, *Nat. Nanotechnol.*, 2012, **7**, 363–368.
3 M. Liu, C. Wang and L. Q. Zhou, *Chin. Phys. B*, 2019, **28**, 037804.
4 L. Sang, J. Hu, R. Zou, Y. Koide and M. Liao, *Sci. Rep.*, 2013, **3**, 2368.

5 F.-X. Liang, J.-Z. Wang, Z.-P. Li and L.-B. Luo, *Adv. Opt. Mater.*, 2017, **5**, 1700081.
6 G. Konstantatos, I. Howard, A. Fischer, S. Hoogland, J. Clifford, E. Klem, L. Levina and E. H. Sargent, *Nature*, 2006, **442**, 180–183.
7 J. Miao, W. Hu, N. Guo, Z. Lu, X. Zou, L. Liao, S. Shi, P. Chen, Z. Fan, J. C. Ho, T.-X. Li, X. S. Chen and W. Lu, *ACS Nano*, 2014, **8**, 3628–3635.
8 Z. Sun, Z. Liu, J. Li, G. Tai, S.-P. Lau and F. Yan, *Adv. Mater.*, 2012, **24**, 5878–5883.
9 J. Li, L. Niu, Z. Zheng and F. Yan, *Adv. Mater.*, 2014, **26**, 5239–5273.
10 C. Xie and F. Yan, *Small*, 2017, **13**, 1701822.
11 M. Buscema, J. O. Island, D. J. Groenendijk, S. I. Blanter, G. A. Steele, H. S. J. van der Zant and A. Castellanos-Gomez, *Chem. Soc. Rev.*, 2015, **44**, 3691–3718.
12 J. Michel, J. Liu and L. C. Kimerling, *Nat. Photonics*, 2010, **4**, 527–534.
13 J. Wang and S. Lee, *Sensors*, 2011, **11**, 696–718.
14 T. Yin, R. Cohen, M. M. Morse, G. Sarid, Y. Chetrit, D. Rubin and M. J. Paniccia, *Opt. Express*, 2007, **15**, 13965.
15 D. Z. Ting, A. Soibel, A. Khoshakhlagh, S. A. Keo, S. B. Rafol, A. M. Fisher, B. J. Pepper, E. M. Luong, C. J. Hill and S. D. Gunapala, *Infrared Phys. Technol.*, 2019, **97**, 210–216.
16 R. W. M. Hoogeveen, R. J. van der A and A. P. H. Goede, *Infrared Phys. Technol.*, 2001, **42**, 1–16.
17 J. Wang, X. Chen, W. Hu, L. Wang, W. Lu, F. Xu, J. Zhao, Y. Shi and R. Ji, *Appl. Phys. Lett.*, 2011, **99**, 113508.
18 P. S. Wijewarnasuriya, Y. Chen, G. Brill, B. Zandi and N. K. Dhar, *IEEE Trans. Electron Devices*, 2010, **57**, 782–787.
19 D. Ban, H. Luo, H. C. Liu, Z. R. Wasilewski, Y. Paltiel, A. Raizman and A. Sher, *Appl. Phys. Lett.*, 2005, **86**, 201103.
20 A. Sharma, B. Bhattacharyya, A. K. Srivastava, T. D. Senguttuvan and S. Husale, *Sci. Rep.*, 2016, **6**, 19138.
21 A. Sharma, A. K. Srivastava, T. D. Senguttuvan and S. Husale, *Sci. Rep.*, 2017, **7**, 17911.
22 B. Bhattacharyya, A. Gupta, T. D. Senguttuvan, V. N. Ojha and S. Husale, *Phys. Status Solidi*, 2018, **255**, 800340.
23 C. Xie, Y. Wang, Z. X. Zhang, D. Wang and L. B. Luo, *Nano Today*, 2018, **19**, 41–83.
24 L.-B. Luo, J.-J. Chen, M.-Z. Wang, H. Hu, C.-Y. Wu, Q. Li, L. Wang, J.-A. Huang and F.-X. Liang, *Adv. Funct. Mater.*, 2014, **24**, 2794–2800.
25 J. Wu, Z. Yang, C. Qiu, Y. Zhang, Z. Wu, J. Yang, Y. Lu, J. Li, D. Yang, R. Hao, E. Li, G. Yu and S. Lin, *Nanoscale*, 2018, **10**, 8023–8030.
26 L.-B. Luo, H. Hu, X.-H. Wang, R. Lu, Y.-F. Zou, Y.-Q. Yu and F.-X. Liang, *J. Mater. Chem. C*, 2015, **3**, 4723–4728.
27 L.-H. Zeng, M.-Z. Wang, H. Hu, B. Nie, Y.-Q. Yu, C.-Y. Wu, L. Wang, J.-G. Hu, C. Xie, F.-X. Liang and L.-B. Luo, *ACS Appl. Mater. Interfaces*, 2013, **5**, 9362–9366.
28 R. Lu, C.-W. Ge, Y.-F. Zou, K. Zheng, D.-D. Wang, T.-F. Zhang and L.-B. Luo, *Laser Photonics Rev.*, 2016, **10**, 595–602.
29 R. D. Mahyavanshi, G. Kalita, A. Ranade, P. Desai, M. Kondo, T. Dewa and M. Tanemura, *IEEE Trans. Electron Devices*, 2018, **65**, 4434–4440.
30 C. Xie, C. Mak, X. Tao and F. Yan, *Adv. Funct. Mater.*, 2017, **27**, 1603886.
31 Z. Sun and H. Chang, *ACS Nano*, 2014, **8**, 4133–4156.
32 Y. Zhao, J. Qiao, Z. Yu, P. Yu, K. Xu, S. P. Lau, W. Zhou, Z. Liu, X. Wang, W. Ji and Y. Chai, *Adv. Mater.*, 2017, **29**, 1604230.
33 W. L. Chow, P. Yu, F. Liu, J. Hong, X. Wang, Q. Zeng, C.-H. Hsu, C. Zhu, J. Zhou, X. Wang, J. Xia, J. Yan, Y. Chen, D. Wu, T. Yu, Z. Shen, H. Lin, C. Jin, B. K. Tay and Z. Liu, *Adv. Mater.*, 2017, **29**, 1602969.
34 A. D. Oyedele, S. Yang, L. Liang, A. A. Puretzky, K. Wang, J. Zhang, P. Yu, P. R. Pudasaini, A. W. Ghosh, Z. Liu, C. M. Rouleau, B. G. Sumpter, M. F. Chisholm, W. Zhou, P. D. Rack, D. B. Geohegan and K. Xiao, *J. Am. Chem. Soc.*, 2017, **139**, 14090–14097.
35 X. Yu, P. Yu, D. Wu, B. Singh, Q. Zeng, H. Lin, W. Zhou, J. Lin, K. Suenaga, Z. Liu and Q. J. Wang, *Nat. Commun.*, 2018, **9**, 1545.
36 C. Yim, K. Lee, N. McEvoy, M. O'Brien, S. Riazimehr, N. C. Berner, C. P. Cullen, J. Kotakoski, J. C. Meyer, M. C. Lemme and G. S. Duesberg, *ACS Nano*, 2016, **10**, 9550–9558.
37 R. Zhuo, L. Zeng, H. Yuan, D. Wu, Y. Wang, Z. Shi, T. Xu, Y. Tian, X. Li and Y. H. Tsang, *Nano Res.*, 2019, **12**, 183–189.
38 L. H. Zeng, S. H. Lin, Z. J. Li, Z. X. Zhang, T. F. Zhang, C. Xie, C. H. Mak, Y. Chai, S. P. Lau, L. B. Luo and Y. H. Tsang, *Adv. Funct. Mater.*, 2018, **28**, 1705970.
39 L. Li, W. Wang, Y. Chai, H. Li, M. Tian and T. Zhai, *Adv. Funct. Mater.*, 2017, **27**, 1701011.
40 C. Yim, N. McEvoy, S. Riazimehr, D. S. Schneider, F. Gity, S. Monaghan, P. K. Hurley, M. C. Lemme and G. S. Duesberg, *Nano Lett.*, 2018, **18**, 1794–1800.
41 L.-H. Zeng, D. Wu, S.-H. Lin, C. Xie, H.-Y. Yuan, W. Lu, S. P. Lau, Y. Chai, L.-B. Luo, Z.-J. Li and Y. H. Tsang, *Adv. Funct. Mater.*, 2019, **29**, 1806878.
42 J. Yuan, T. Sun, Z. Hu, W. Yu, W. Ma, K. Zhang, B. Sun, S. P. Lau, Q. Bao, S. Lin and S. Li, *ACS Appl. Mater. Interfaces*, 2018, **10**, 40614–40622.
43 L. Zeng, S. Lin, Z. Lou, H. Yuan, H. Long, Y. Li, W. Lu, S. P. Lau, D. Wu and Y. H. Tsang, *NPG Asia Mater.*, 2018, **10**, 352–362.
44 Z.-X. Zhang, L.-H. Zeng, X.-W. Tong, Y. Gao, C. Xie, Y. H. Tsang, L.-B. Luo and Y.-C. Wu, *J. Phys. Chem. Lett.*, 2018, **9**, 1185–1194.
45 S. M. Sze and K. K. Ng, *Physics of Semiconductor Devices*, 2007.
46 L. Wang, J. Jie, Z. Shao, Q. Zhang, X. Zhang, Y. Wang, Z. Sun and S.-T. Lee, *Adv. Funct. Mater.*, 2015, **25**, 2910–2919.
47 X. Li, M. Zhu, M. Du, Z. Lv, L. Zhang, Y. Li, Y. Yang, T. Yang, X. Li, K. Wang, H. Zhu and Y. Fang, *Small*, 2016, **12**, 595–601.
48 C. Xie, L. Zeng, Z. Zhang, Y. H. Tsang, L. Luo and J. H. Lee, *Nanoscale*, 2018, **10**, 15285–15293.
49 D. Wu, Y. Wang, L. Zeng, C. Jia, E. Wu, T. Xu, Z. Shi, Y. Tian, X. Li and Y. H. Tsang, *ACS Photonics*, 2018, **5**, 3820–3827.
50 J.-A. Huang and L.-B. Luo, *Adv. Opt. Mater.*, 2018, **6**, 1701282.
51 C. Xie, B. Nie, L. Zeng, F.-X. Liang, M.-Z. Wang, L. Luo, M. Feng, Y. Yu, C.-Y. Wu, Y. Wu and S.-H. Yu, *ACS Nano*, 2014, **8**, 4015–4022.
52 J. W. Suk, A. Kitt, C. W. Magnuson, Y. Hao, S. Ahmed, J. An, A. K. Swan, B. B. Goldberg and R. S. Ruoff, *ACS Nano*, 2011, **5**, 6916–6924.